Low energy electron transmission through layered materials and chiral organic films
Neu, P.S.

Citation
Neu, P. S. (2024, June 12). *Low energy electron transmission through layered materials and chiral organic films*. Retrieved from https://hdl.handle.net/1887/3762501

4 SYMMETRIES OF ELECTRON INTERACTIONS WITH hBN-GRAPHENE HETEROSTACKS

4.1 Introduction

Stacking two different van der Waals (vdW) materials produces a heterostructure that breaks the out-of-plane symmetry of the sample [1]. The graphene-hBN heterostack is commonly used in experiments, where hBN provides an insulating flat surface for the graphene with a minimal lattice mismatch [2,3]. Placing the graphene on or between hBN is known to yield better transport characteristics (e.g., higher electron mobility [4–6] and superconductivity in twisted bilayer graphene [7]) than on other common substrates like silicon or silicon nitride. It is generally assumed that the coupling of hBN to the graphene can be neglected at the Fermi level, as hBN is a large band gap insulator [8,9].

Like graphene, hBN is a vdW material with a hexagonal lattice, with each boron (B) atom bonding to three nitrogen (N) atoms in plane and vice versa. Unlike in transition metal dichalcogenides (TMDs), the B and the N atoms in hBN lie in the same plane. Following the interference toy model we applied for graphene layers [10], one can hence expect interlayer states in multilayer hBN, and even in a graphene-hBN heterostack.

Jobst et al. [11] have previously investigated hBN interlayer states using LEEM. They showed splitting of the hBN interlayer states for two to five layers of hBN on silicon, similar to the case of two to five layers of graphene. Furthermore, they presented calculations explaining that few-layer graphene on *bulk* hBN retains its characteristic splitting of the interlayer state, while few-layer graphene on few-layer hBN should show a mixed interlayer state.

Hibino et al. [12] have reported on mono- and bilayer graphene on top of mono- and bilayer hBN on a Cobalt (Co) surface. They measured LEEM-IV spectra showing a characteristic interlayer state minimum even for one layer graphene on one layer hBN, and a splitting of the minimum upon adding more layers of graphene and/or hBN.

In this chapter, we discuss measurements on a hBN-on-graphene heterostructure sample that is suspended over the 2-μm holes of a TEM grid. We present LEEM- and eV-TEM-IV spectra of this free-standing heterostructure and compare these to the previously published reports. The combination of transmission and reflection data allows us to determine elastic and inelastic path lengths for the electrons, as a function of their energy. The fact that the sample is prepared on a TEM grid also allows us to investigate the role of symmetry. We can flip the sample and measure LEEM and eV-TEM spectra on the reversed order of layers.

4.2 Results

4.2.1 Geometry and images

The hBN-on-graphene heterostack is prepared by the polymer-free transfer method [13] using hBN and graphene grown on copper (Cu) by chemical vapor deposition (CVD) (purchased from Graphene Laboratories [14] and Graphenea [15], respectively). The graphene on Cu is floated on an ammonium persulfate (APS) solution until the Cu is etched away and the graphene is picked up with the hBN-on-copper substrate. The resulting graphene-hBN-Cu stack is then flipped and the copper is again etched away by the APS solution. The floating hBN-graphene

stack is then picked up by a SiN holey TEM grid [16] brought in contact from the top. The sample fabrication is illustrated in more detail in the appendix Figure 4.A1.

In the usual orientation of the TEM grid, i.e., with the flat side towards the LEEM objective lens, the resulting order of layers as seen from the LEEM objective lens-side is: hBN (on top of) / graphene (on top of a holey) / SiN TEM grid. The graphene and the hBN layers are sandwiched together with the sides that had been in contact with copper before facing outwards.

Previous inspection of the CVD-grown materials by LEEM has shown that there are multilayer areas of elongated folds or tears in the graphene and triangular multilayer areas in the hBN.
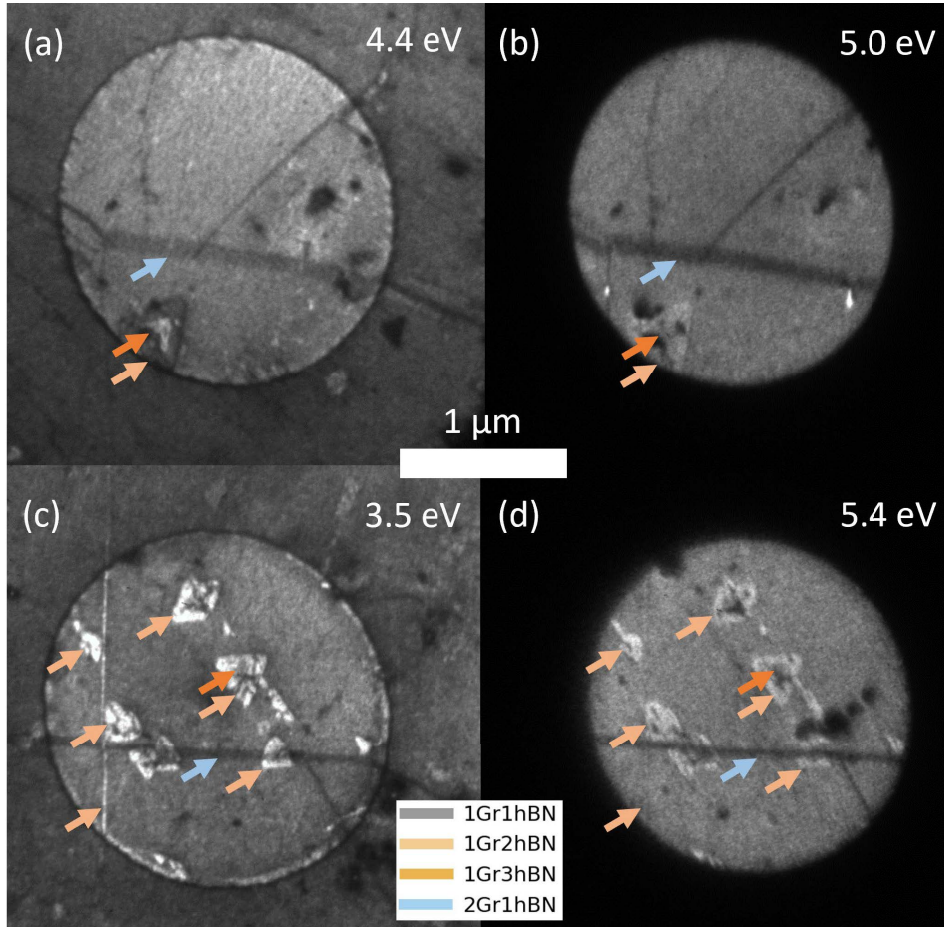
Figure 4.1: LEEM images (a, c) and eV-TEM images (b,d) of the hBN-on-graphene heterostack. While most areas are covered with one layer of hBN on top of one layer of graphene, some triangles of additional layers of hBN and lines of additional graphene layers show. The Pt/Pd-coated SiN support grid is impenetrable for the electrons and roughens the layered material on top of it, compared to the free-standing areas. The arrows point to areas with an additional layer of graphene (2Gr1hBN) and additional layers of hBN (1Gr2hBN and 1Gr3hBN). The other areas are one layer of hBN on one layer of graphene (1Gr1hBN).

The LEEM and eV-TEM images of the heterostructure on top of a TEM grid hole (see Figure 4.1) show multilayer areas that have characteristic shapes for either graphene or hBN. Firstly, there are long stripes pointed out by the blue arrows in Figure 4.1, that have the same shape as stripes previously seen in graphene-only samples and are thus ascribed to folds and tears in the graphene. (We will confirm the layer count below by comparing the spectra to the previous

publication of Hibino et al. [12].) Secondly, the triangles marked by orange arrows are characteristic for hBN grown by CVD. Previous inspection of the hBN on copper, as used for the transfer, revealed the presence of multilayer triangles. Furthermore, the continuity between these multilayer areas also shows that the majority of the sample is covered by a monolayer of graphene with a monolayer of hBN on top, denoted as 1Gr1hBN.

We note that the free-standing area is more reflective than the area supported by the Pt/Pd coated TEM grid throughout the energy range. This is similar to what we have previously seen for graphene samples and is attributed to a higher flatness of the free-standing area [17,18]. The images shown in Figure 4.1 are part of an energy scan up to 30 eV electron energy recorded with a contrast aperture (equivalent diameter ~0.3 Å^{-1} for LEEM and ~0.6 Å^{-1} for eV-TEM) placed around the specular spot.
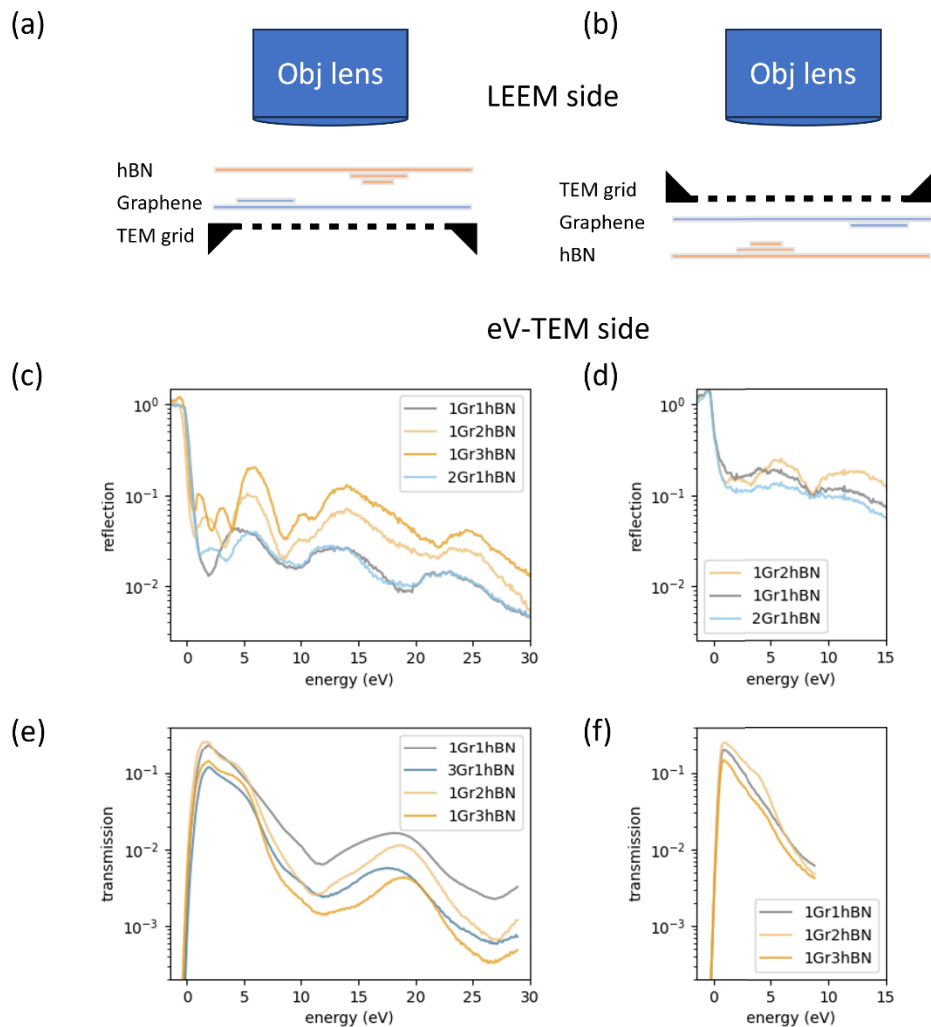
Figure 4.2: Sketch of the graphene-hBN heterostack sample with (a) the original orientation (reflection from the hBN side), with the reflection spectra (c) and transmission spectra (e) measured in this configuration. For the subsequent measurements the sample was flipped as shown in (b) (reflection from the graphene side) and the reflection/transmission spectra (d) and (f), respectively, were acquired in this flipped orientation.

The option of flipping the sample allows us to acquire four spectra on the same sample. These four spectra cover all possibilities of perpendicular electron transmission and reflection of the sample. In the left column of Figure 4.2, we show the spectra recorded in the usual configuration (with the hBN side towards the LEEM lens as sketched in Figure 4.2a), with the reflection spectra in Fig. 4.2c) and the transmission spectra in Fig. 4.2e). In the right column of Figure 4.2, the spectra recorded in the flipped configuration (with the graphene side towards the LEEM lens as sketched in panel b) are depicted, with reflection and transmission spectra in panel 2d) and 2f), respectively.

The spectra d) and f) acquired with the flipped geometry are cut off at 15 and 10 eV, respectively, as the spatial resolution, especially limited by astigmatism, does not allow for distinguishing between the areas of different layer count at higher energies. The imaging conditions are inherently worse in the flipped condition, as the holey silicon nitride (SiN) membrane is recessed into the SiN frame. Since the potential difference from the sample to the electron lens is much larger on the LEEM side (15 kV) than on the eV-TEM side (~200 V), the electric equipotential surfaces close to the TEM grid are much more curved, when the recessed (instead of the flat side) of the TEM-grid is facing the LEEM side. The curved equipotential surfaces, i.e., the in-plane electric field, deflect the electrons when imaging an area that is not the center of the TEM grid. The deflection can be compensated to some degree by tilting the sample (relative to the LEEM lens), adjusting the centering on the aberration correcting mirror, and – in the LEEM and not the eV-TEM case – adjusting the incidence angle of the electrons. However, these compensations are optimized at a low energy and get worse with increasing energy.

4.2.2 Spectra

When we concentrate on the spectra recorded in the original orientation first (Figure 4.2 c/e), some general trends are visible upon adding more layers of graphene and hBN. We will name them here, before discussing them in more detail:

1. Increased reflectivity and decreased transmissivity with an increasing number of layers.
2. Splitting of the band at 0-5 eV with every added layer and graphene/hBN dependent shift.
3. Development of the hBN-specific minima that correspond to a band at 8-11 eV upon adding hBN layers.
4. Graphene/hBN dependent shift of the ~20 eV band.

First, the reflectivity is increasing with an increasing number of layers, whereas the transmissivity is decreasing. This is expected in a framework of elastic and inelastic mean free paths (MFPs). The transmissivity has to generally decrease with layer count, as electrons are scattered inelastically with a certain probability in each layer. With a constant inelastic mean free path (λ_{IMFP}), the flux of electrons not intercepted by inelastic scattering decreased exponentially, as $T \propto \exp(-d/\lambda_{\text{IMFP}})$. The reflectivity increases with layer count (at least far from the bands), as the electrons can elastically reflect from every layer with a certain probability. As we have argued in the toy model based on interference of the wave function (see Chapter 3), the reflected electron will undergo multiple elastic scattering processes in

between the layers, producing the interlayer states. But this is a higher order effect, so it is true that reflectivity generally increases with layer count.
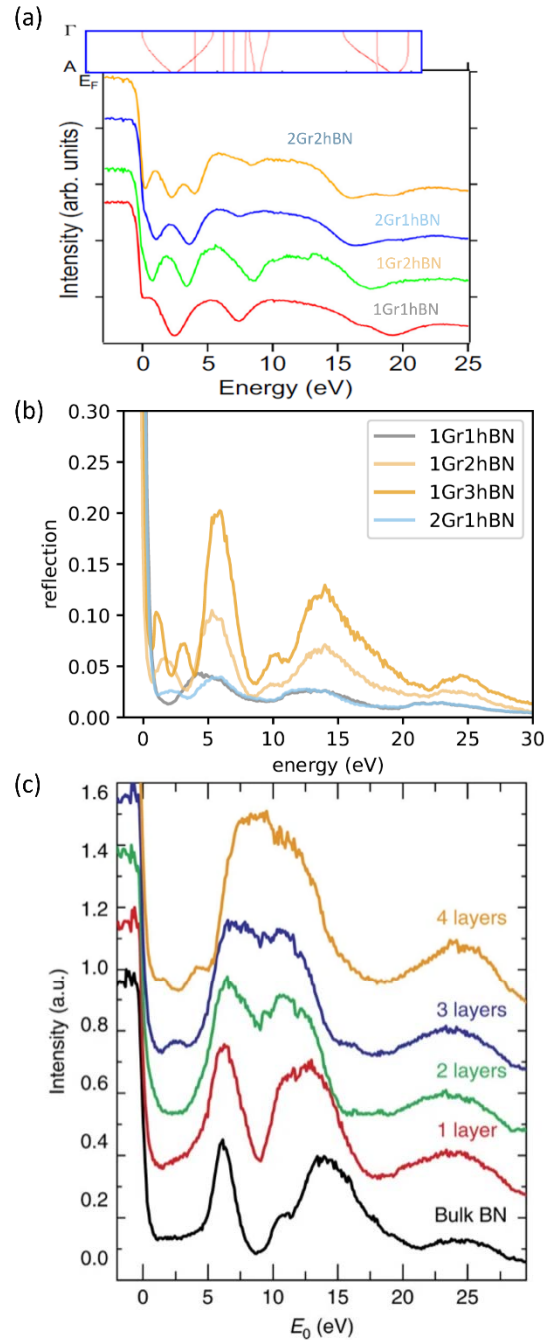
Figure 4.3: Comparison of LEEM spectra of (b) our hBN-on-graphene to previously reported non-free-standing graphene by (a) Hibino et al. [12] and (c) Jobst et al. [11]. Hibino et al measured graphene (CVD grown on Cu and transferred) on top of hBN grown on Co. Jobst et al. measured few-layer exfoliated graphene on top of bulk hBN. The inset in (a) shows the band structure of a periodically continued graphene-hBN heterostack (along the out-of-plane direction).

Still, it is notable, that the increase in reflectivity in Figure 4.2c is small for an added layer of graphene, i.e., the 2Gr1hBN curve, and comparably large for added layers of hBN, i.e., the

1Gr2hBN curve. The same small effect has been seen in the graphene-only samples in Chapter 3.

Second, the splitting of the low energy interlayer state is visible in both LEEM and eV-TEM. In the LEEM spectra, the energy resolution is sufficient for counting of the total number of layers. The number of minima only depends on the number of layers, not whether these are graphene or hBN layers. Like in graphene, there are $n-1$ minima for n layers. Nevertheless, the energies of the interlayer states shift depending on whether more graphene or hBN is added, as we will discuss later with help of Figure 4.4.

In the eV-TEM spectra the splitting of the interlayer state leads to a striking situation, where the transmissivity of the 1Gr2hBN stack oscillates around the transmissivity of the 1Gr1hBN stack, i.e., the transmissivity increases at 2 eV and 5 eV upon adding a layer of hBN, although the electrons have to pass three layers as opposed to two in the 1Gr1hBN case. This example shows how important it is to distinguish between elastic and inelastic MFP. In a material that is dominated by inelastic scattering, a thicker sample would always have a lower transmissivity.

We highlight that the existence and splitting of the interlayer state is evidence for the cleanliness of the graphene-hBN interface. The surfaces that are brought in contact with the polymer-free transfer method are the top surfaces that were exposed to air and have not undergone specific cleaning steps. Thus, these interlayer states can also be expected in other vdW heterostructure devices.

Third, the hBN-specific band at 8-11 eV becomes more pronounced with an increased layer count of hBN. This band is known from the bulk hBN data and calculations, e.g., [11,12,19–21], and does not exist in graphene (compare [22,23]). In the LEEM spectrum, it is visible for the data with only one layer of hBN and splits in two distinguishable dips for more layers of hBN. [it is not discernible in the eV-TEM spectrum].

Fourth, the band around 20 eV, that manifests itself in the data as a minimum in reflectivity and a maximum in transmissivity, shifts to lower energy for more graphene-like heterostacks and to higher energy for more hBN-like heterostacks. The state is seen in both (bulk) graphene and (bulk) hBN. In our interference toy model, it is the result of the second order interference (whereas the 0-5 eV split band results from the first order interference), and thus an interlayer state. No layer-dependent splitting of the state is visible, which is attributed to increased inelastic scattering at higher energies. We will discuss this shift in more detail when comparing to the data of Hibino et al. [12] in Figures 4.3 and 4.4.

The reflection spectra (in the original orientation) are reprinted in Figure 4.3b, alongside the spectra published by Hibino et al. [12] and Jobst et al. [11], in Figures 4.3a and 4.3c, respectively, on an aligned energy scale. While our sample consists of hBN on graphene, the other publications report on graphene on hBN. Thus, the hBN-specific minimum in their spectra is cloaked by the addition of more graphene on top [24]. Also, in the LEEM spectrum in Figure

4.2 d the cloaking effect is visible. It is clear that, if the total MFP of the probing electron is in the order of a few layers, the top layer will have the largest contribution to the reflectivity, whereas the layers past the MFP barely contribute to the reflectivity.

Furthermore, all the spectra in Figure 4.3 show the second order interference state, that shifts with addition of graphene or hBN, and the first order interference state. The 0-5 eV band from Hibino et al. shows the same number of splittings as our data, only depending on the number layers. In the data of Jobst et al., the splitting of the state only depends on the number of graphene layers, with $n - 1$ minima for n graphene layers. While this appears contradictory, they show in their Figure 4.4b [11], how the interference pattern between graphene and hBN develops into a pattern of only the few layer graphene, upon increasing the hBN layer count from 5 to 22 and applying a Gaussian broadening to mimic the energy resolution of the setup.
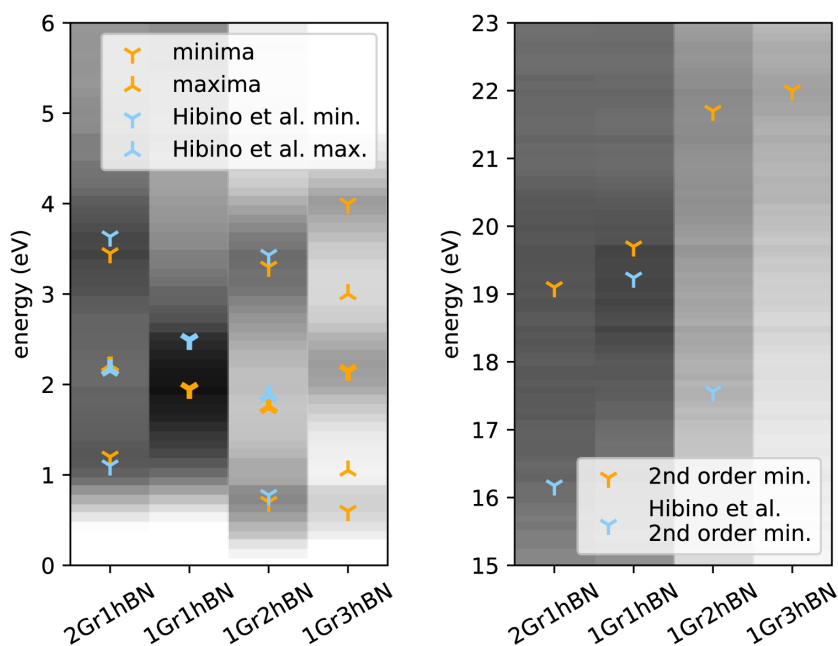
Figure 4.4: Energy shift of the reflectivity minima and maxima of different graphene/hBN combinations as found in our data and by Hibino et al. [12]. The measured spectra of each layer count (see Figure 4.2c) are shown in the grayscale in the background. A splitting and shift are seen in the low-energy interlayer state (a, 0-5 eV). The central minimum/maximum is printed bold for orientation. The second interlayer state (b, around 20 eV) also shifts depending on the hBN/graphene likeness of the heterostack.

To discuss the shift of the minima/maxima upon addition of graphene or hBN, we plot the minima and maxima energies in Figure 4.4, for our data and the data by Hibino et al. The energy of the interlayer states shifts depending on whether more graphene or hBN is added to the 1Gr1hBN heterostack.

For the 0-5 eV band (see Figure 4.4a) in our data, the maximum of the 1Gr2hBN spectrum is shifted to ~0.3 eV lower than the minimum of the 1Gr1hBN spectrum, whereas the 2Gr1hBN spectrum is shifted to ~0.2 eV higher energy. Also, the mirror mode transition is shifted to lower energy in the more hBN-like stacks (see Figure 4.3b), indicating a lowering of the work

function, as the Fermi levels are aligned. In the data of Hibino et al. (see Figure 4.3a), the 1Gr2hBN interlayer and 2Gr1hBN states resemble our states, shifting to lower energy for more hBN (Figure 4.4a). However, the 1Gr1hBN minimum does not lay on that line, suggesting that the Co substrate shifts the states compared to our free-standing sample. In LEEM, the effect of the Co substrate on the spectra will decay with increasing thickness of the samples.

The band around 20 eV, with the minima plotted in Figure 4.4b, shifts to lower energy for more graphene-like heterostacks and to higher energy for more hBN-like heterostacks. This trend is also visible in the spectra from Jobst et al. [11], that are reprinted in Figure 4.3c, for more layers of graphene added on top of bulk hBN. In the spectra by Hibino et al. [12] (reprinted in Figure 4.3a) however, the band moves to lower energy irrespective of whether graphene or hBN is added. We attribute this to the fact that the Gr/hBN minimum in Hibino et al.'s data is already higher than in our data (~ 21 eV), probably caused by the Co substrate in their experiment. Also, as Hibino et al. are considering graphene on hBN, one can expect that the graphene top layer dominates the LEEM spectrum. However, like in the 0-5 eV band, that 1Gr1hBN data seems to be the outlier, with the 2Gr1hBN band at higher energy than the 1Gr2hBN band, as in our data.

4.2.3 Calculated spectra and electron density distributions

As the experimental spectra are acquired on free-standing areas, they are free of substrate effects and especially suited for comparison to calculations. The electron density and the resulting reflectivity were calculated by our collaborator Eugene E. Krasovskii by constructing the Bloch eigenfunctions from matching augmented plane waves for a periodic continuation of the respective heterostack [25,26]. The calculated reflection spectra for the 1Gr1hBN, 1Gr2hBN, and 2Gr1hBN stacks are shown in Figure 4.5. R(E) is the reflected intensity in the specular spot, thus directly comparable to the LEEM data. By comparison to experiment, the work function was fitted to be $\Phi = E_{\text{vac.}} - E_{\text{F}} \approx 4.3$ eV. We note that no loss is applied, implying that – as long as no diffracted beams are formed – all electrons are either reflected or transmitted. The calculated reflection spectra of the flipped heterostacks coincided with the original orientation except for numerical errors, thus they are not shown in Figure 4.5. We will discuss how losses break this symmetry later (see section 4.2.5).

The projected electron densities in Figure 4.6 actually differ for the two different orientations of a stack. The color in each plot shows the electron density, thus the absolute square of the electron wave function (Bloch eigenfunction) at a given energy. As the calculation is done in three dimensions, the electron density is projected onto the out-of-plane dimension. The horizontal axis shows the out-of-plane dimension, with the electrons incident from the right, and the position of each layer marked. The transmission states show up as maxima on the left side of the sample, characteristic maxima inside the sample, and minima on the right side, the reflection side, of the sample.

We will discuss the spectra (Fig. 4.5) and the electron density (Fig. 4.6) in conjunction, following the order of features as discussed previously for the experiments.

Firstly, the lowest energy reflectivity minimum that is related to the first interference state shows an energy shift depending on the added material. Like in our experiment, the state seen

for 1Gr1hBN splits and shifts to lower energy upon the addition of a layer of hBN or splits and shifts to higher energy upon the addition of a layer of graphene. The electron density of the state is centered in between the layers, as is expected for the interference state, but also has some electron density in the layer, with more in the hBN than in the graphene layer.
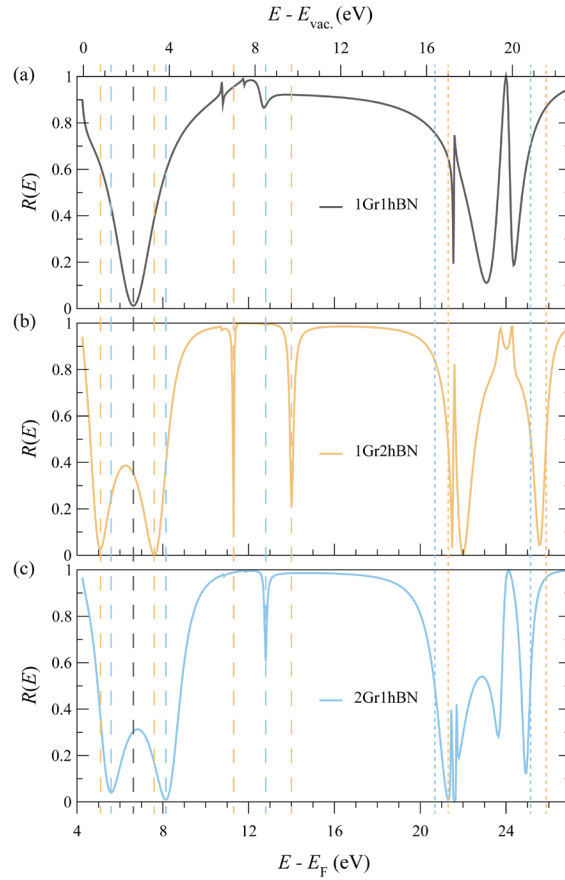
Figure 4.5: Calculated reflectivity of the bilayer and the two different trilyayer stacks in the specular spot without loss. The low energy reflectivity minima are marked with dashed lines in the corresponding colors to compare their energies. For the bands above 20 eV (with respect to E_F) the dotted lines indicate the energies of 50% reflectivity, as we can only resolve a general broad minimum at that high energy in experiment. The energy shifts of the low energy minima, the splitting of the ~13 eV minimum, and the general shift of the broad high energy minimum are also seen in experiment, compare Fig. 4.2c and Fig. 4.4. Calculations by E.E. Krasovskii.

Secondly, the hBN-specific state around E = 9 eV with respect to $E_{vac.}$ ($\approx E_F + 13$ eV) shows up as one minimum in the 1Gr1hBN and 2Gr1hBN spectra, i.e., the spectra that have one hBN layer, and as two minima in the 1Gr2hBN spectrum. Other experiments [11,12,19] and calculations [12,20,27] on multilayer hBN also show two reflection minima. In all the heterostacks the electron density associated with these states is not centered in the layers, but shows as three maxima in between the layers, resembling a $3p_z$ orbital. Independent of the orientation, the majority of the electron density is shifted towards the hBN layers, indicating that these states are hBN-specific.
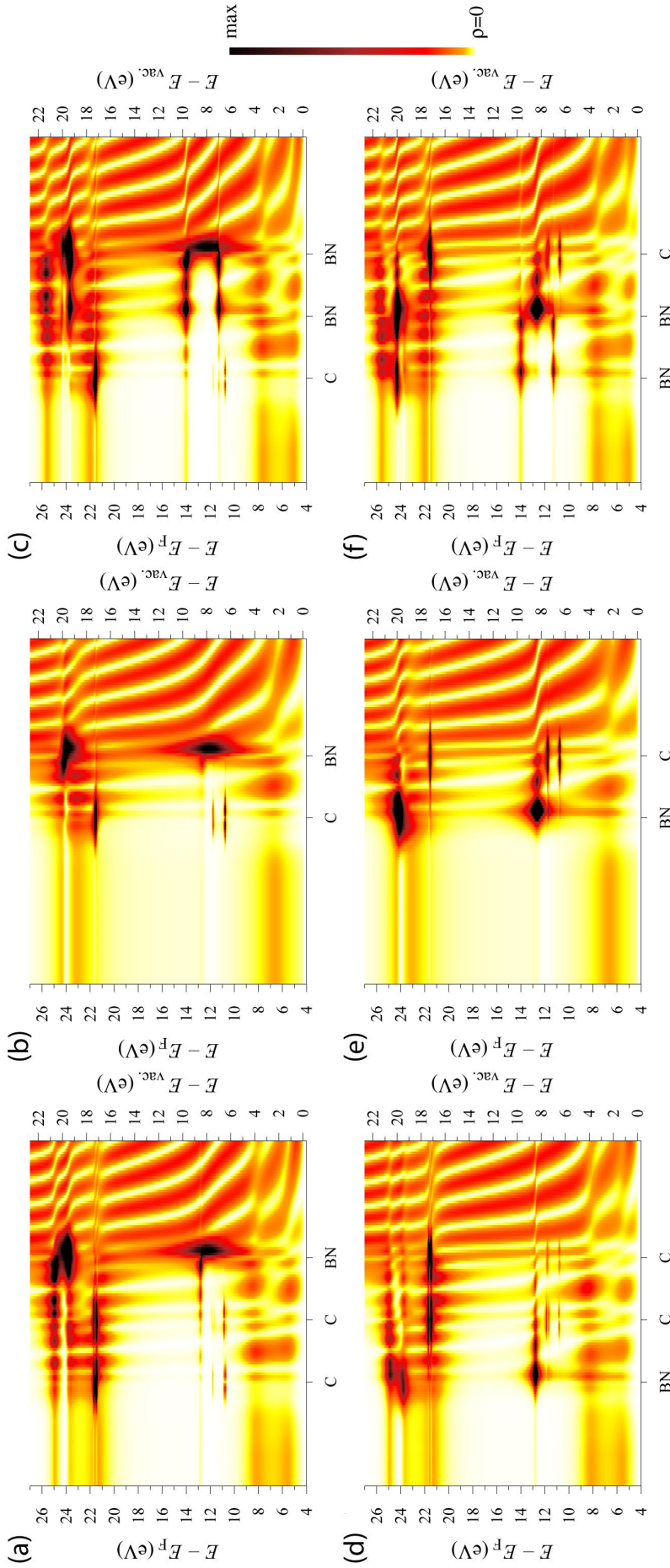
Figure 4.6: Projected electron density ρ in the LEED state for the 2Gr1hBN (a,d), 1Gr1hBN (b,e) and 1Gr2hBN (c,f) stacks. The horizontal axis is the out-of-plane dimension with the positions of the hBN layers (BN) and graphene layers (C) marked. The energy scale refers to the Fermi energy E_F, while the experimental spectra are given with respect to the vacuum level $E_{vac} = E_F + \Phi$, with the work function $\Phi \approx 4.3$ eV. The electron wave is incident on the sample from the right side, thus the interference of the incident and reflected wave is visible on the right of the sample, with the wavelength shortening with increasing energy. The top row shows stacks with the hBN side facing the electron source, the bottom row shows stacks with the graphene side facing the electron source. Flipping the stack did not affect the calculated reflectivity. Calculations by E.E. Krasovskii.

The splitting of the hBN-specific state is different from the splitting of the first interference state at 3 eV. This is seen in the energy width of the minima, which is much narrower than for the interference states, and the fact that the minima do not split further for more than two layers of hBN. The calculated band structure of the graphene/hBN superstructure by Hibino et al. [12] (1Gr1hBN, Figure 4.3a) already shows the state at 11 eV, but it does not affect electron reflectivity as it has practically zero dispersion, so the electrons cannot couple into the state. For multilayer hBN, the bands are dispersive, and thus show up in the electron reflection spectra as minima.

Thirdly, the calculations show that the broad reflection minimum at 17 to 22 eV ($\approx E_F + 21$ to $26\,\text{eV}$) consists of multiple minima that shift and split depending on the composition of the heterostack. The individual minima and maxima are not resolved in the experiment as inelastic scattering is large at these high energies. The range of these combined bands is indicated in the Figure 4.5 by dotted lines in the respective color at 50% reflectivity. Inelastic scattering shortens the lifetime of the state and thus broadens it in energy. The sharpest minimum followed by a maximum at ~21.5 eV, which are too narrow to be measured, is caused by the formation of the first-order diffraction beams.

The shift of this broadened band, as marked by the dotted lines at 50% reflectivity, follows the same systematics as in the experiment: it shifts to lower energy for the addition of graphene and to higher energy for the addition of hBN. However, the shift between the 2Gr1hBN and the 1Gr2hBN stack is only 0.8 eV, compared to ~3 eV in the experiment (c.f. Fig. 4.3b). We attribute this to inelastic scattering, which is not included in the calculation, and the resulting short inelastic mean free path (IMFP). In LEEM, the probing depth is limited to the order of the IMFP (which we will see is less than 1 layer at this high energy), thus the spectrum will be dominated by the material the electrons are first incident on – in this case the hBN. The LEEM spectrum at this energy thus resembles the bulk hBN spectrum (see Fig. 4.3) more than the lossless calculation.

This reasoning of finite probing depth is supported by the electron density plots (Fig. 4.6). The lower energy state ($E_F + 21.5$ eV) making up this broad reflection minimum is centered in the graphene layers, while the higher energy states ($E_F + 23.5$ to 26 eV) are dominant around the hBN layers, independent of heterostack composition and side of electron incidence. Including inelastic losses, we can thus expect to probe more of the states closer to the incidence side of the LEEM electrons. The graphene-dominated states are centered in the layer, with two side-lobes in between two layers, while the highest energy ($E_F + 25$ to 26 eV) hBN-dominated state has 4 density maxima in between the layers, like non-overlapping $3p_z$ orbitals around each layer. In the trilayer stacks (Fig. 4.6a,c,d,f) the lower hBN-dominated/heavy state ($E_F + 24.2$ eV in Fig. 4.6f and $E_F + 23.7$ eV in the other trilayers) is centered in the outermost hBN layer and avoids the graphene layers.

4.2.4 Elastic and inelastic mean free paths

A quantitative understanding of the elastic and inelastic MFP can be gained from fitting the toy model to the data. For this, the effective mass in the dispersion relation was first adapted to match the first-order interlayer state between the model and the reflection data. To give an

intuition for the spectra produced by the interference toy model, we plot the reflection and transmission spectra calculated for constant reflectivity r²=0.2 and a loss factor β exponentially decreasing with wavevector k (see Fig. 4.7a-b, including caption). The hBN-specific state around 10 eV is not accounted for in this simple model, as it is not an interference state and already exists in the monolayer [21] (see Fig. 4.6).

The calculation of MFPs is done for the experimental spectra taken in the original orientation of the sample, for the areas with a monolayer of graphene below and one, two, and three layers of hBN on top. For comparison, also the monolayer graphene data from Chapter 3 is included. Fitting the parameters r and β, in the toy model to the reflectivity and transmissivity at each energy and layer count yields the parameters shown in Figures 4.7 c and d. In this fit, we apply the same r and β for graphene and hBN. As the fit has zero degrees of freedom, the best fit matches the data. Later, we will change the toy model to include different parameters for different layers.
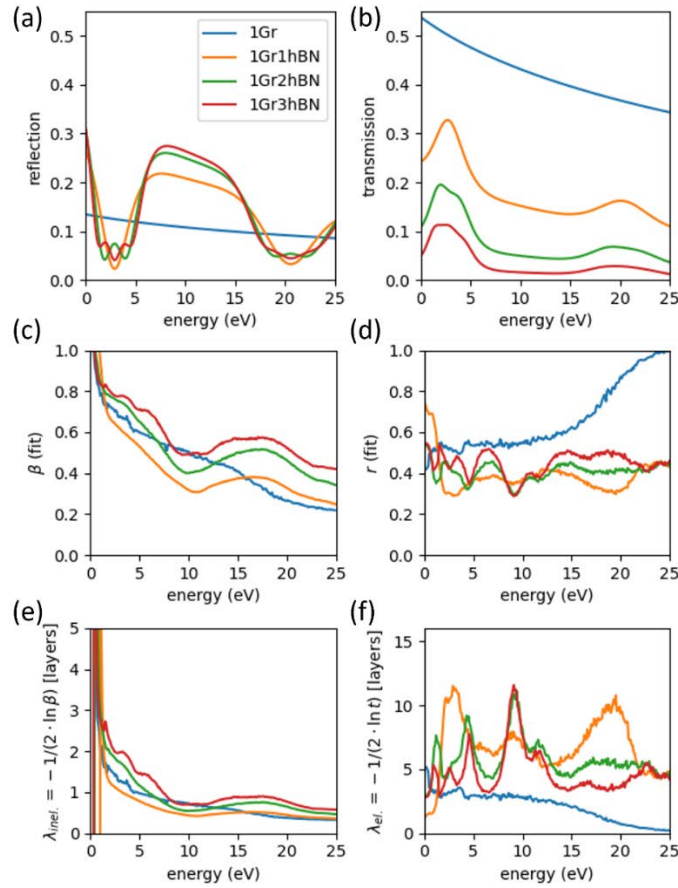
Figure 4.7: The reflection (a) and transmission (b) spectra for the toy model used at fixed $r^2 = 0.2$ and exponentially decreasing β do not account for the hBN-specific band around 10 eV. Fit parameters β (c) and r (d) obtained by fitting the model (for each energy independently) to the hBN-on-graphene heterostack data, in analogy to the analysis in chapter 3. The inelastic MFP (e) and elastic MFP (f) are obtained from the fit parameters.

The inelastic and elastic MFPs (Figure 4.7 e and f) are calculated from the fit parameters via $1/\lambda_{\mathrm{inel.}} = -2\ln\beta$ and $1/\lambda_{\mathrm{el.}} = -2\ln t$ with $t^2 = 1 - r^2$. Generally, the inelastic MFP is

found to decrease with energy from approximately 3 layers at 1 eV to 0.5-1 layers at 25 eV, with a broad minimum around 10 eV (except for monolayer graphene). Alike other features discussed before, this minimum shifts to lower energy with increasing number of hBN layers (best visible in the plot of β). While the low-energy interferences are invisible in the 1Gr1hBN and 1Gr2hBN inelastic MFPs, meaning that the interferences are well accounted for in the toy model, the 1Gr3hBN inelastic MFP does show remnants of the three-fold split minimum. In fact, the minima are sharper in the data than in the toy model. As the spacing of the split minima is connected to the broadness of the band in the A- Γ direction, this means our toy dispersion relation $E(k)$ is not rising steep enough in this region.

The elastic MFPs of all the graphene-hBN heterostacks are larger than the one of monolayer graphene throughout the 2-25 eV energy range, with maxima of about 10 layer counts (Fig. 4.7f). Like in the 1Gr3hBN inelastic MFP curve, some remnants of the interference minima below 5 eV mismatching the toy model are visible in the elastic MFP curve.

In Fig. 4.7f), the hBN-specific band shows up as a maximum in the elastic MFP of all the heterostacks. For 2 and 3 layers of hBN on graphene two distinct, sharp maxima (that match well between the two curves) at 8 eV (~12 layer counts high) and 12 eV (~7 layer counts high) are visible. For the 2 and 3 layers of hBN on graphene the peak at 8 eV is the global maximum. It can be expected that this feature corresponding to the hBN specific band shows up as a maximum in MFP, as it is not accounted for in the toy model. In fact, the associated reflection maximum falls into the maximum region of the toy model visualized in Figure 4.7a. Still, our method correctly assigned it to an elastic feature, as it should, being a band structure feature rather than an inelastic feature. In a modified toy model, one could retrieve the 10 eV hBN-specific band as a beating pattern between a boron and a nitrogen layer of different electron-optical density, i.e., different effective electron mass. That way, the increased inelastic MFP at that energy would be absorbed into the model.

4.2.5 Symmetry upon flipping the sample

Finally, we turn to the (transmission) data gathered on the flipped sample. Although the geometry presents some problems to the electron-optical alignment as discussed before, we can discuss the effect of reversing the direction of travel of the electrons through the sample. Firstly, we highlight that reversing the direction of the incoming electrons, as sketched in Figure 4.8, is not exactly the same as time-reversal. When we reverse time in the scattering experiment, it would look like the reflected electron beam and the transmitted electron beam are travelling towards the sample and interfere to create the incoming electron beam. This would not see a reflected beam on the other side of the sample, as it is the case for reversing the sample.

For the case without inelastic scattering or loss, however, the transmitted and reflected electron flux in the flipped sample should follow time-reversal symmetry. The solution of the [time-independent] Schrödinger equation for the right-incident electron beam can be constructed from a linear combination of the stationary state solution of the left-incident electron beam and its complex conjugate. An instructive calculation found in [28,29] shows, that the wave-function transmissivity is the same and the reflectivity only differs by a phase-factor upon flipping the incoming electron direction, for an arbitrary potential going to vacuum level at a finite distance

from the sample. I.e., we expect that the real-valued transmissivity T and reflectivity R of electrons is the same for the flipped sample.

In practice, we will have to consider inelastic scattering as well. In that case, an asymmetric sample with thickness larger than or comparable to the MFP will not show the same reflectivity on both sides. Think of a silicon chip with a typical thickness of ~1 mm with graphene deposited on one side. On that side, we would expect to measure a graphene signal in LEEM, whilst only a Si signal is expected at the other side.
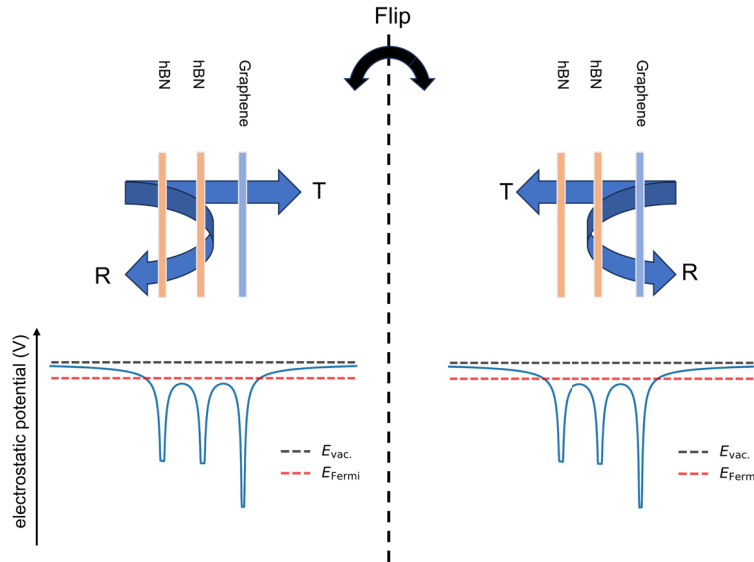
Figure 4.8: Illustration of the electrostatic potential the electron experiences upon reflection/transmission. Flipping the sample is the same as reversing the direction of the incoming electrons. The question is: Does the reflected/transmitted electron flux depend on the direction of travel of the electron?

To get a proper intuition for the problem, we again use the interference toy model introduced in Chapter 3. This model can easily be modified to allow for different reflectivity r (and the connected transmissivity t), loss factor β and phase propagation φ (caused by thickness or effective electron mass) in the hBN and graphene layers. The transmission and reflection resulting from changes in (combinations of) these parameters are shown in Figures 4.9 and 4.10 and discussed below.

Firstly, we set the parameters for reflectivity r, the connected transmissivity t, and loss factor β are to different values for hBN and graphene layers, while the phase propagation is kept the same for both hBN and graphene. For the graphene layer we choose the same values as in Figure 4.7 a/b, but for hBN, we choose $r_{hBN}^2 = 2 \cdot r_{Gr}^2$ and $\beta_{hBN} = \sqrt{\beta_{Gr}}$, i.e., a doubled electron reflectivity and a doubled inelastic MFP. In Figure 4.9 we show the resulting curves. Clearly, upon reversing the order of layers, the transmission spectra stay the same, as expected. However, while the reflection spectra show the same qualitative features related to interlayer resonances, there is a clear difference between both symmetries. The features measured with graphene at the LEEM-lens side (top side) are much sharper than for the flipped configuration.

The reason for that is that the electron interaction with the underlying layers is diminished by the higher r and β in the hBN layer.
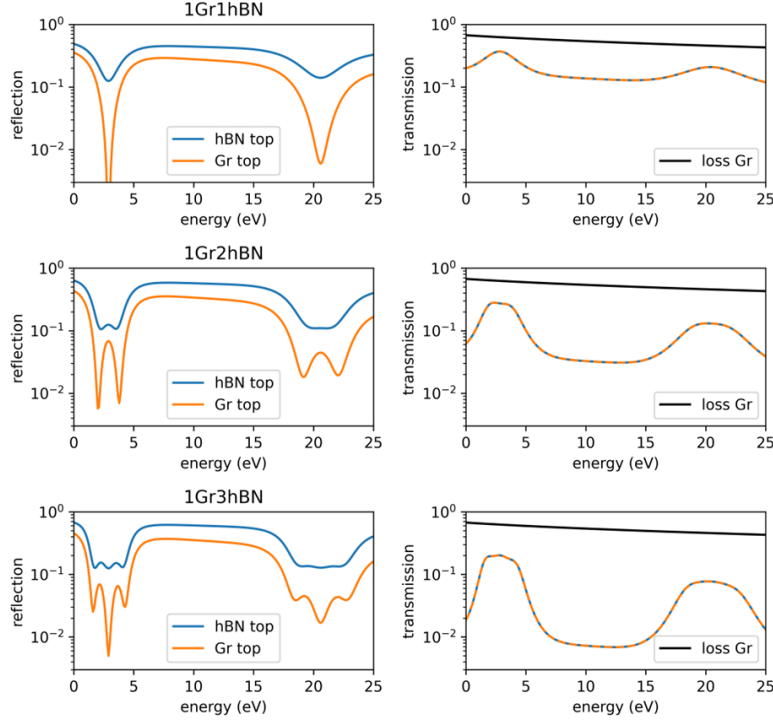
Figure 4.9: Calculated toy-model reflection and transmission spectra for multiple hBN layers on top of one graphene layer (blue) and the flipped stack (orange). Calculation where graphene and hBN are assumed to have different inelastic MFP and reflectivity, while the phase propagation over a unit cell is kept the same. The reflected spectrum changes upon flipping the sample, while the transmitted spectrum is invariant (dashed lines). The chosen energy dependent intensity loss factor β^2 for graphene is plotted in black.

Next, we also change the phase propagation φ, while keeping all other parameters (r and β) the same as in Figure 4.9. In Figure 4.10, the phase propagation φ_{hBN} in hBN is altered from the phase propagation in the graphene layers by calculating φ_{hBN} for a hBN layer spacing that is 1% thinner than that of graphene. This emulates the difference of out-of-plane lattice vector, that is ~1% between hBN and graphene [30]. These modifications do result in different transmission curves upon flipping the sample, as shown in Fig. 4.10. In fact, the transmission maxima are shifted now, albeit only by a small amount. The reflection minima however move significantly by ~1 eV. Also, the series of minima for 1Gr2hBN and 1Gr3hBN are not symmetric any longer (cf. Fig. 4.9), with the lower-energy minima diving lower in the case of Gr topped stacks. This may be expected, as the split minima are more hBN-like or more graphene-like, and we set the IMFP in hBN to be twice the value in graphene. As a larger IMFP increases the number of elastic reflections (comparable to an increased finesse in an optical cavity), a larger IMFP will lead to sharper interference features. E.g., for 2Gr1hBN (in the original hBN-on-top configuration), the central reflectivity maximum is formed by the minimum of the underlying 2Gr (i.e., zero in wave function) not destructively interfering with the wave reflected from the top 1hBN. Equivalently, one can think of it as the result of the top 1Gr1hBN layer minimum not interfering with the reflection from the bottom 1Gr layer. Then

the minima on either side of that maximum are more influenced by either the interference of the wave reflected from the 2Gr interfering with the wave reflected from the 1hBN or the wave reflected from the final Gr layer and 1Gr1hBN on top.
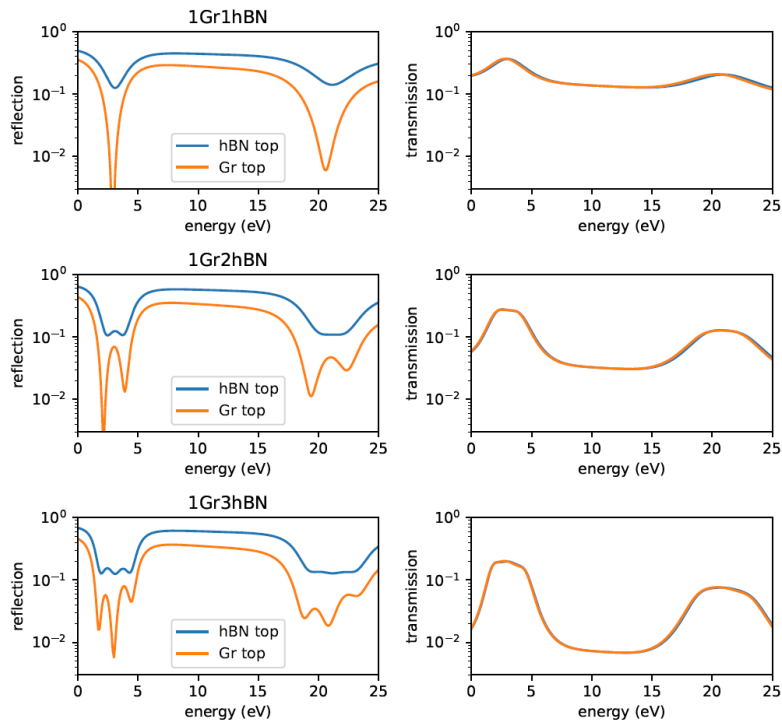
Figure 4.10: Calculated toy-model reflection and transmission spectra for multiple hBN layers on top of one graphene layer (blue) and the flipped stack (orange). In addition to the loss and reflectivity changed in Figure 4.7, the phase propagation is calculated for a 1% thinner hBN unit cell. The transmission spectra show a slight shift in flipping the sample and the split reflection minima lose their symmetry.

Having considered these models for transmission and reflection of flipped samples, and concluding that flipping the sample should have little influence on the transmission, we revisit the experimental transmission data in Figure 4.2 d/f. While the transmitted electron flux is in the same range for both orientations, the flipped sample is more transmissive in the thicker 1Gr2hBN area than in the thinner 1Gr1hBN area over the large 1 to 6 eV energy range. This unexpected peculiarity is present throughout the flipped sample, as shown in the real space images in Figure 4.11. This increased transmissivity cannot be explained in any of the previous modifications of the toy model.

Hence, our data are most probably influenced by the experimental setup used and specifically by the supporting TEM grid chosen. The graphene-hBN sample is suspended over the 2 μm holes on a 70 nm thick SiN membrane, that is flat on the top but recessed 200 μm into the frame from the bottom side [16]. The measurement setup has a much stronger electric field of ~10 kV/mm on the LEEM side than on the eV-TEM side, with ~50 V/mm, leading to highly distorted equipotential lines in the flipped sample, where the recessed holes point to the LEEM side. While we expect that the field strengths are not sufficient to significantly gate the sample (which is barely possible in vacuum), we expect distortions of the electron paths, focusing the

(incoming) electron bundle. Furthermore, we know that due to the described challenges to alignment in the flipped sample, the electrons were not measured at straight incidence and exit angle. In a band structure picture, this means the measurements display a contour/cut along a path in in $E - k_\parallel$ space that is not the $k_\parallel = 0$ cut, i.e., not the cut along the Γ symmetry axis. In case that cut is (partially) following the parabolic-like band dispersion, this can explain the broad energy range with high transmissivity.
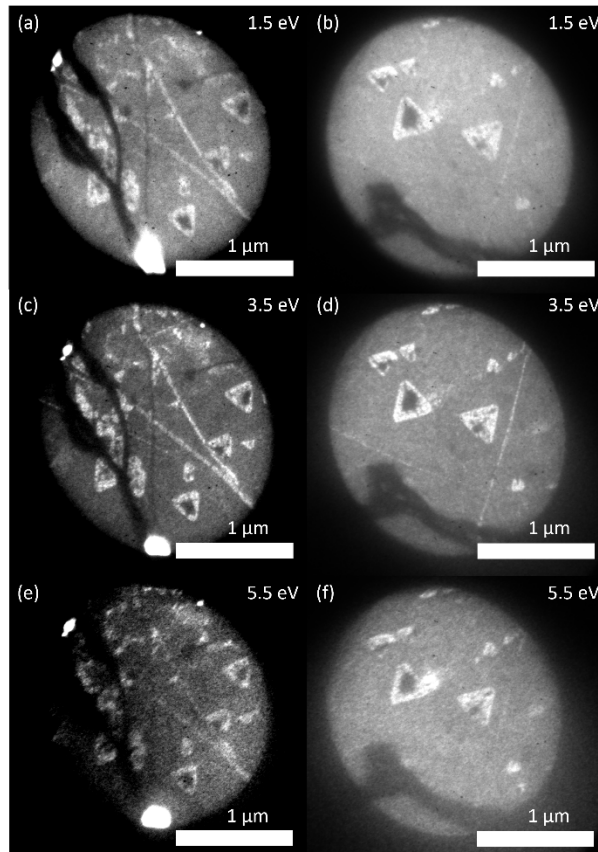
Figure 4.11: eV-TEM images of two areas of the flipped sample. The triangles with an additional hBN layer are more transmissive than the thinner 1Gr1hBN areas surrounding them over an unexpectedly broad energy range (also see Figure 4.2 f). Symmetry considerations for the graphene-hBN stack do not allow for this difference in transmissivity upon flipping the sample, so the difference must be sought in the geometry of the sample, including the TEM grid, and the resulting asymmetric electric fields.

Finally, practical implications of the sample preparation are likely to increase the transmissivity in the hBN-triangle areas. The additional layer increases the stiffness and likely the flatness in the triangle area. A flatter surface is expected to have higher coherence of the reflected and transmitted wave function, thus improving the interference conditions.

4.3 Conclusion

To conclude, we have shown how the low electron energy reflectivity and transmissivity spectra of a freestanding graphene-hBN heterostructure depend on both the layer count and the order

of the layers. As these areas are independent of substrate influences, they are especially suited for comparison to theory. The interlayer states splitting around 1-4 eV show that there is a direct interaction of the graphene and hBN layers that is predicted in our interference toy model. Hence, contamination between both layers must be minimal.

While the bands of hBN at energies below 5 eV (and above the vacuum level) can be explained in analogy to graphene, one cannot neglect the hBN-specific band around 10 eV that builds up with increasing hBN layer count. If one does not incorporate it in the interference toy model, the band shows up as an increase in elastic MFP in the fitted MFPs.

While the differences between reflection from the graphene and the hBN side of the heterostack are captured in the toy model, the differences in the transmission curves measured are stronger than explainable in the toy model. While the electron transmission and reflection coefficients in fully elastic scattering from a potential are invariant under flipping the electron direction, the introduction of loss in the toy model allows for asymmetry, albeit small in transmission for realistic reflection and loss coefficients.

Our research shows, that there is likely interaction with the hBN substrate in many prepared vdW samples, at least at the energies we probe. The graphene-hBN heterostacks measured may in turn serve as high-transmissivity substrates for eV-TEM investigation of layers that grow better on hBN than graphene, e.g., pentacene [31], or be used to encapsulate a sample in between. Improvements to the measurement, especially in the flipped-sample geometry, may come from additional alignment degrees of freedom of the eV-TEM gun. Adding a deflector to control the incidence angle of the eV-TEM electron bundle would allow for angle-resolved transmitted-electron spectra measurements, complementary to ARRES and ARPES.

Appendix

Sample fabrication

The sample is prepared by applying the polymer-free transfer method [13] to graphene and hBN. The steps are illustrated in Figure 4.A1.
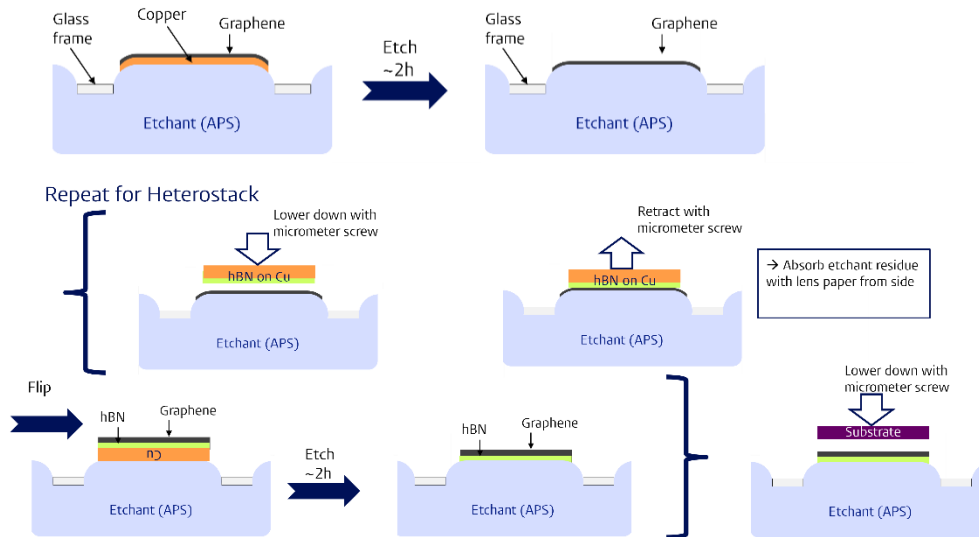
Figure 4.A1: Sample fabrication for a hBN on graphene heterostructure on a TEM grid (substrate).

The first step is the same as for the graphene on TEM grid samples.

0. Gently place a square glass frame (6 mm x 6 mm inner square) on top of the 0.5 M ammonium persulfate (APS) solution. The frame is only floating due to surface tension, thus curving the etchant surface.

1. Cut a 5 mm x 5 mm square of flat graphene on copper (round scalpel blade) and place it on top of the APS inside the glass frame.

2. Wait until the copper is fully etched away (approx. 2 h). Only the edge of the floating graphene is visible by eye, if it is not crumbled.

3. Cut a 5 mm x 5 mm square of flat hBN on copper. Fix it to a vertical micrometer screw and lower it down onto the floating graphene. After making contact, retract the screw and blot away excess APS solution droplets from the side.

4. Flip the hBN on copper, with the picked-up graphene, and float the copperside inside the glass frame.

5. Wait another 2 hours, until the copper is etched away fully.

6. Lower down the holey SiN TEM grid (sputter-coated with 5 nm Pt/Pd from each side) by a micrometer screw, until it is in contact with the floating hBN/graphene stack. Move the micrometer screw with the TEM grid attached to the side and retract it until the surface tension of the APS breaks. The connection to the TEM grid should break towards the side, to not stress the free-standing graphene-hBN membranes. Blot away excess APS droplets from the side of the TEM grid chip.

Flipped sample

To flip the sample, it is taken out of the ESCHER setup vacuum and re-mounted in its holder. To find back the same area on the sample, it is most convenient to use eV-TEM, as the eV-TEM electron beam illuminates most of the TEM grid (compared to a few micrometers in the LEEM bundle).

The eV-TEM images at a large field of view in the usual and flipped configuration are shown in Figure 4.A2. The brightest features ar holes that are not covered with graphene or hBN, thus do not impede the electrons. Especially the vertical row of uncovered holes is recognizable when identifying the same area. Other features are connected by orange arrows in Figure 4.A2. Note that the flipping the TEM grid upside down results in a mirrored image.
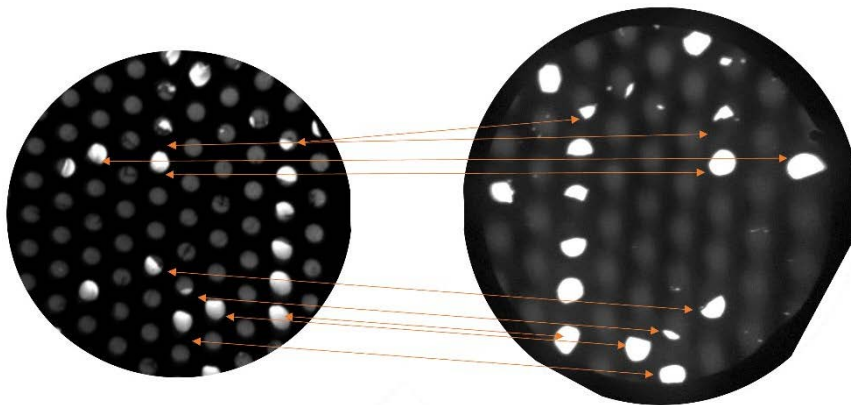
Figure 4.A2: Large-scale eV-TEM images of the same sample area in the original (a) and flipped (b) orientation. Some select features are highlighted in both images, to show the symmetry. Like when flipping an overhead projector transparency upside down, the outlines are mirrored.

Free-standing hBN

In addition to the graphene-hBN heterostructure, we also prepared a sample with only hBN [15] on a TEM grid. A LEEM image of that sample is shown in Figure 4.A3. The hBN areas that are supported by the Pt/Pd coated TEM grid are possible to image, as they can drain the LEEM electrons that are absorbed. As hBN is an insulator, the free standing hBN areas accumulate charges as soon as the LEEM electron bundle illuminates them.

In Figure 4.A3 the sample was move to the right in two steps, thus the part on the right has been exposed to the electron beam for longer. Whereas the free-standing part on the left can still be imaged in LEEM, the central part has charged up so far, that the incident electrons at 14.4 eV are repelled before they reach the sample. Thus, the holes in the center appear to be in mirror mode. The hBN on the middle hole is starting to rip.

The hBN on the holes on the right, that has been exposed to the LEEM electron bundle for the longest, has ripped, under the force of the accumulated charge in the LEEM magnetic field. For an estimate of the mechanical breaking strength of hBN see [32].
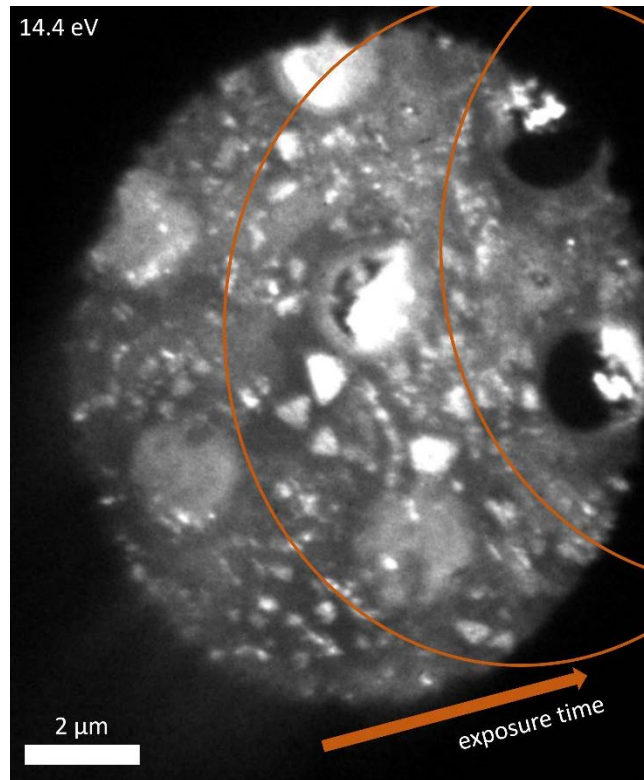
Figure 4.A3: LEEM image of hBN (mostly monolayer grown on Cu) on top of a Pt/Pd coated TEM grid. On the free-standing areas the electrons cannot be drained, as hBN is an insulator, an effect known as charging. After a few seconds of exposure to the electron beam, the free-standing hBN deforms and finally rips. The sample was moved under the beam from right to left, meaning that the free-standing hBN on the left has been exposed the longest and is starting to rip.

References

[1]   A.K. Geim, I. V Grigorieva, Van der Waals heterostructures., Nature 499 (2013) 419–25. https://doi.org/10.1038/nature12385.

[2]   A. Ramasubramaniam, D. Naveh, E. Towe, Tunable band gaps in bilayer transition-metal dichalcogenides, Phys. Rev. B - Condens. Matter Mater. Phys. 84 (2011) 1070–1075. https://doi.org/10.1103/PhysRevB.84.205325.

[3]   J. Wang, F. Ma, W. Liang, M. Sun, Electrical properties and applications of graphene, hexagonal boron nitride (h-BN), and graphene/h-BN heterostructures, Mater. Today Phys. 2 (2017) 6–34. https://doi.org/10.1016/j.mtphys.2017.07.001.

[4]   C.R. Dean, A.F. Young, I. Meric, C. Lee, L. Wang, S. Sorgenfrei, K. Watanabe, T. Taniguchi, P. Kim, K.L. Shepard, J. Hone, Boron nitride substrates for high-quality graphene electronics, Nat. Nanotechnol. 5 (2010) 722–726. https://doi.org/10.1038/nnano.2010.172.

[5]   L. Wang, I. Meric, P.Y. Huang, Q. Gao, Y. Gao, H. Tran, T. Taniguchi, K. Watanabe, L.M. Campos, D.A. Muller, J. Guo, P. Kim, J. Hone, K.L. Shepard, C.R. Dean, One-Dimensional Electrical Contact to a Two-Dimensional Material, Science (80-.). 342 (2013) 614–617. https://doi.org/10.1126/science.1244358.

[6]   L. Martini, V. Mišeikis, D. Esteban, J. Azpeitia, S. Pezzini, P. Paletti, M.W. Ochapski, D. Convertino, M.G. Hernandez, I. Jimenez, C. Coletti, Scalable High-Mobility Graphene/hBN Heterostructures, ACS Appl. Mater. Interfaces 15 (2023) 37794–37801. https://doi.org/10.1021/acsami.3c06120.

[7]   Y. Cao, V. Fatemi, S. Fang, K. Watanabe, T. Taniguchi, E. Kaxiras, P. Jarillo-Herrero, Unconventional superconductivity in magic-angle graphene superlattices, Nature 556 (2018) 43–50. https://doi.org/10.1038/nature26160.

[8]   R.M. Torres-Rojas, D.A. Contreras-Solorio, L. Hernández, A. Enciso, Band gap variation in bi, tri and few-layered 2D graphene/hBN heterostructures, Solid State Commun. 341 (2022) 114553. https://doi.org/10.1016/j.ssc.2021.114553.

[9]   J. Jung, A.M. Dasilva, A.H. Macdonald, S. Adam, Origin of band gaps in graphene on hexagonal boron nitride, Nat. Commun. 6 (2015) 1–11. https://doi.org/10.1038/ncomms7308.

[10]   P.S. Neu, D. Geelen, R.M. Tromp, S.J. van der Molen, Extracting transverse electron mean free paths in graphene at low energy, Ultramicroscopy 253 (2023) 113800. https://doi.org/10.1016/j.ultramic.2023.113800.

[11]   J. Jobst, A.J.H. van der Torren, E.E. Krasovskii, J. Balgley, C.R. Dean, R.M. Tromp, S.J. van der Molen, Quantifying electronic band interactions in van der Waals materials using angle-resolved reflected-electron spectroscopy, Nat. Commun. 7 (2016) 13621. https://doi.org/10.1038/ncomms13621.

[12]   H. Hibino, S. Wang, C.M. Orofeo, H. Kageshima, Growth and low-energy electron microscopy characterizations of graphene and hexagonal boron nitride, Prog. Cryst. Growth Charact. Mater. 62 (2016) 155–176. https://doi.org/10.1016/j.pcrysgrow.2016.04.008.

[13]   X. Zhang, C. Xu, Z. Zou, Z. Wu, S. Yin, Z. Zhang, J. Liu, Y. Xia, C. Te Lin, P. Zhao, H. Wang, A scalable polymer-free method for transferring graphene onto arbitrary surfaces, Carbon N. Y. 161 (2020) 479–485. https://doi.org/10.1016/j.carbon.2020.01.111.

[14]   Graphene Laboratories, Single layer h-BN (Boron Nitride) Film grown on Copper Foil, (2022). https://www.graphene-supermarket.com/products/single-layer-h-bn-boron-nitride-film-grown-on-copper-foil-2-x-1 (accessed May 28, 2022).

[15]   Graphenea, Monolayer Graphene on Cu, (2020). https://www.graphenea.com/collections/buy-graphene-films/products/monolayer-graphene-on-cu-4-inches?variant=276514394 (accessed November 7, 2023).

[16]   Ted Pella Inc., PELCO® Silicon Nitride Support Films for TEM, Prod. Overv. (2011). https://www.tedpella.com/grids_html/silicon-nitride-holey.aspx (accessed November 2, 2023).

[17]   S. Chen, M. Horn Von Hoegen, P.A. Thiel, M.C. Tringides, Diffraction paradox: An unusually broad diffraction background marks high quality graphene, Phys. Rev. B 100 (2019) 1–6. https://doi.org/10.1103/PhysRevB.100.155307.

[18]   M.K.L. Man, S. Deckoff-Jones, A. Winchester, G. Shi, G. Gupta, A.D. Mohite, S. Kar, E. Kioupakis, S. Talapatra, K.M. Dani, Protecting the properties of monolayer MoS2 on silicon based substrates with an atomically thin buffer, Sci. Rep. 6 (2016) 1–9. https://doi.org/10.1038/srep20890.

[19]   P.C. Mende, Q. Gao, A. Ismach, H. Chou, M. Widom, R. Ruoff, L. Colombo, R.M. Feenstra, Characterization of hexagonal boron nitride layers on nickel surfaces by low-energy electron microscopy, Surf. Sci. 659 (2017) 31–42. https://doi.org/10.1016/j.susc.2017.02.004.

[20]   L. Schué, L. Sponza, A. Plaud, H. Bensalah, K. Watanabe, T. Taniguchi, F. Ducastelle, A. Loiseau, J. Barjon, Bright Luminescence from Indirect and Strongly Bound Excitons in h-BN, Phys. Rev. Lett. 122 (2019). https://doi.org/10.1103/PhysRevLett.122.067401.

[21]   C. Herrmann, P. Omelchenko, K.L. Kavanagh, Growth of h-BN on copper (110) in a LEEM, Surf. Sci. 669 (2018) 133–139. https://doi.org/10.1016/j.susc.2017.11.021.

[22]   H. Hibino, H. Kageshima, F. Maeda, M. Nagase, Y. Kobayashi, Y. Kobayashi, H. Yamaguchi, Thickness Determination of Graphene Layers Formed on SiC Using Low-Energy Electron Microscopy, E-Journal Surf. Sci. Nanotechnol. 6 (2008) 107–110. https://doi.org/10.1380/ejssnt.2008.107.

[23]   D. Geelen, J. Jobst, E.E. Krasovskii, S.J. van der Molen, R.M. Tromp, Nonuniversal Transverse Electron Mean Free Path through Few-layer Graphene, Phys. Rev. Lett. 123 (2019) 086802. https://doi.org/10.1103/PhysRevLett.123.086802.

[24]   T.A. de Jong, T. Benschop, X. Chen, E.E. Krasovskii, M.J.A. de Dood, R.M. Tromp, M.P. Allan, S.J. van der Molen, Imaging moiré deformation and dynamics in twisted bilayer graphene, Nat. Commun. 13 (2022). https://doi.org/10.1038/s41467-021-27646-1.

[25]   E.E. Krasovskii, Augmented-plane-wave approach to scattering of Bloch electrons by an interface, Phys. Rev. B 70 (2004) 245322. https://doi.org/10.1103/PhysRevB.70.245322.

[26]   E. Krasovskii, Ab Initio Theory of Photoemission from Graphene, Nanomaterials 11 (2021) 1212. https://doi.org/10.3390/nano11051212.

[27]   Y. Malozovsky, C. Bamba, A. Stewart, L. Franklin, D. Bagayoko, Accurate Ground State Electronic and Related Properties of Hexagonal Boron Nitride (h-BN), J. Mod. Phys. 11 (2020) 928–943. https://doi.org/10.4236/jmp.2020.116057.

[28]   K. Konishi, G. Paffuti, The Schrödinger equation, in: Quantum Mech., Oxford University PressOxford, 2009: pp. 49–88. https://doi.org/10.1093/oso/9780199560264. 003.0003.

[29]   G.D. Mahan, 10. Scattering Theory, in: Quantum Mech. a Nutshell, Princeton University Press, 2009: pp. 320–351. https://doi.org/10.1515/9781400833382-011.

[30]   J. Wang, F. Ma, M. Sun, Graphene, hexagonal boron nitride, and their heterostructures: properties and applications, RSC Adv. 7 (2017) 16801–16822. https://doi.org/10.1039/ C7RA00260B.

[31]   A. Tebyani, Probing molecular layers with low-energy electrons, Casimir PhD series, 2024, https://doi.org/1887/3721791.

[32]   A. Falin, Q. Cai, E.J.G. Santos, D. Scullion, D. Qian, R. Zhang, Z. Yang, S. Huang, K. Watanabe, T. Taniguchi, M.R. Barnett, Y. Chen, R.S. Ruoff, L.H. Li, Mechanical properties of atomically thin boron nitride and the role of interlayer interactions, Nat. Commun. 8 (2017) 1–9. https://doi.org/10.1038/ncomms15815.